Nedjari, H. Daaou; Guerri, O.; Saighi, M.

Article

Full rotor modelling and generalized actuator disc for wind turbine wake investigation

Energy Reports

Provided in Cooperation with:
Elsevier

Suggested Citation: Nedjari, H. Daaou; Guerri, O.; Saighi, M. (2020) : Full rotor modelling and generalized actuator disc for wind turbine wake investigation, Energy Reports, ISSN 2352-4847, Elsevier, Amsterdam, Vol. 6, Iss. 3, pp. 232-255, https://doi.org/10.1016/j.egyr.2019.10.041

Available online at www.sciencedirect.com
ScienceDirect
Energy Reports 6 (2020) 232–255
www.elsevier.com/locate/egyr

Tmrees, EURACA, 04 to 06 September 2019, Athens, Greece

Full rotor modelling and generalized actuator disc for wind turbine wake investigation

H. Daaou Nedjari[a,*], O. Guerri[a], M. Saighi[b]

[a] *Centre de Developpement des Energies Renouvelables, CDER, 16340, Algiers, Algeria*
[b] *Thermodynamics and Energetical Systems Laboratory, Faculty of Physics, USTHB, B.P 32 El Alia, 16111 Bab Ezzouar-Algiers, Algeria*

Received 19 September 2019; accepted 28 October 2019

Abstract

This paper purpose a numerical study of the flow downstream a wind turbine erected in the neutral atmospheric boundary layer. A first part consists of unsteady wind flow simulations through a full moving rotor, which lets identifying the vortex generated in the wind turbine wake. The governed equations were solved in two sub-domains (Rotor/Stator) and the moved fluid flow continuity at the domain interface was managed by the *Sliding Mesh* technique of *Turbo-machinery* implemented in an open-source 'Code _Saturne'. However, the unsteady full rotor calculations proved to be extensive and inadequate for optimizing the wind farm layout. Therefore, to achieve a more accessible wake model, the second part consists of the design of a generalized hybrid wake model in which, contrary to the full simulation, an actuator disc 'with non-zero thicknesses' has substituted the rotor and was coupled to the Reynolds averaged Navier Stokes equations (RANS) through additional source terms. The modified k-ε was used to model the turbulence developed downstream the rotor. The ability of the proposed model to represent the wake was demonstrated by a series of validations with experimental data and results were in good agreement.

Peer-review under responsibility of the scientific committee of the Tmrees, EURACA, 2019.

Keywords: U-RANS; Sliding Mesh; Generalized actuator volume; CFD

1. Introduction

According to numerous studies, the rotation of the wind turbine rotor during the energy conversion process is causing significant perturbation of the flow by generating turbulent structures that weaken the wind speed behind the rotor where circular vortexes are detached at tip blades and are progressively extend downstream to form a cylindrical shear layer denoting the wake [1,2]. In the case of an isolated wind turbine, the shear zone moves gradually to form the far wake and merge with the atmospheric boundary layer. However, as wind farms consist of several wind turbines rows, the highly disturbing wind wake will be perceived as an inflow by downwind turbines. In this case, the turbulence increasing expands the aerodynamic loads that affect the proper functioning of downstream machines and can cause the turbine damage. Indeed, it has been shown that the most modern wind farms today record

* Corresponding author.
E-mail address: h.daaou@cder.dz (H. Daaou Nedjari).

https://doi.org/10.1016/j.egyr.2019.10.041

Peer-review under responsibility of the scientific committee of the Tmrees, EURACA, 2019.

Nomenclature

A	rotor area
a	axial induction
B	blade number
c	blade cord
Ct, Cd, Cl	thrust, drag and lift coefficient
$C\nu$, $C\varepsilon 1$, $C\varepsilon 2$	model Constants
D, R	rotor diameter and radius
dr	radial element blade
D, L	drag and lift forces
H:	hub height
It	turbulence Intensity
K	Von Karman constant
k	kinetic turbulent energy
u, v, w	instantaneous velocity
U_0	reference velocity at the hub high
Ux, Ut	axial and tangential velocity
U_{rel}	relative velocity
F	Total force
Fx, Ft	normal and tangential forces
α, β	local angle of attack and pitch angle
Ω	angular speed
ε	dissipation rate
λ	tip-speed ratio
ν, $\nu\tau$	cinematic and turbulent viscosity
ρ	air density
Re	Reynolds number
S_Φ, $S_{t\Phi}$, $S_{p\Phi}$	source term

energy losses ranging from 10 to 20% caused by the wind turbines wake [3,4] and the wind farm installation success remains essentially based on wake modelling and its impact on neighbouring wind turbines. Indeed, to limit the uncertainties and risks, the development of large-scale wind farm projects requires understanding the wake effects to improve the wind farms output. However, because of the multiple turbulences magnitudes, which are more or less important at different positions on the farm, the wake modelling remains challenging and complex to achieve. Several models have been developed in literature to answer this problem. Crespo et al. 1999 [5] and Vermeer et al. 2003 [6] have presented an in-depth review on this topic and gave a vigorous description of the wind turbine wake with the different approaches so far used to evaluate the wake impact in wind farm. Hansen 2006, [4] and Troldborg 2007 [7] have also provided a complement of the developed methods to estimate the aerodynamics loads in rotor models. Later, Sanderse et al. 2011 [8] classified the different techniques used in two most important categories, namely the engineering method and the hybrid-actuator disc method coupled to the RANS or LES techniques. T. Göçmen et al. 2016 [9], presented concisely a synthesis of the several models developed at the DTU University of Denmark and J. Thé et al. 2017 [10] have exposed a detailed comparison of hybrids RANS-LES models applied to the wake study.

The synthesis has revealed that the most used BEM approach [6,11] allows to describe the flow deficit downstream the wind turbine but it does not give accurate information on the wake flow behaviour. In other hands, the full computational fluid dynamics (CFD) methods provide detailed information mainly for the near wake but require the representation of the exact rotor shape and need much larger CPU time [2,4,8]. An intermediate method

is to model the wind turbine rotor as the force acting on the wind through an actuator disc combined with the CFD technique. Indeed, Mikkelsen and Sorensen [7,12] suggested modelling the rotor in the wind farm without exactly representing the blades geometries. They have introduced the rotor by an actuator line model expressing the forces applied to the flow. Dobrev et al. [13] have determined the forces by the BEM theory and have represented the rotor by actuator surfaces. This technique, also known by Virtual Blade Momentum (VBM) method was introduced in Ansys Fluent12 and used by A. Makridis [14] for the wake over complex topographies assessment. The more simplified model remains the actuator disc concepts that introduce the rotor effects on the flow thought the axial and tangential forces. J.N. Sørensen et al. [15,16] used the actuator disc to solve the wake of an isolated wind turbine in a uniform laminar flow, using a cylindrical formulation of the Navier Stokes equations. C. Masson et al. [17] and I. Ammara et al. [18], in 2001, introduced the axisymmetric formulation developed by Ainslie [19] to the actuator disc concept. C. Alinot et al. in 2003 [20], C. Sibuet Watters et al. in 2008 [21] and A. El Kasmi et al. in 2008 [22] have also used the actuator disc model in a two-dimensional and axisymmetric formulation and considered different thermal stratification conditions. In order to improve the actuator disc results, A. El Kasmi and Masson [22] introduced an additional term in the turbulent kinetic energy transport equation. They applied the rotor model to a disc of zero thickness using the fluent industrial software. The wake predicted by A. El Kasmi and C. Masson was compared with the experimental data and showed a very good agreement thanks to the consideration of additional dissipation terms, which allowed the improvement of the axis-symmetric actuator disc model. Still with the aim of improving wake prediction in wind farm, the present study purpose, in second part, a simplified hybrid generalized wake model 'without any change in the dissipation rate'. The proposal is to model the influence of the wind rotor on the flow as distributed forces on an actuator volume whose width represents the thickness of the wind turbine blade. The rotor model is then coupled to the Navier Stokes equations implemented in an open-source code.

However, in order to better understand the wake structure phenomenon, this work first focuses on 3D modelling of the full rotor based on the U-RANS-CFD simulation. It consists in solving the Navier Stokes equation in a field built around a physical rotor blade in a rotating frame. Sørensen and Hansen [23], Sørensen and Johansen [24] and Zahle [25] have studied the modelling of the complete rotor using the RANS decomposition with different turbulence models, such as k-ε and sst-Kω. To deal with the interface between the static and the moving part in the fluid field domain, this study introduced the transient *Sliding Mesh* model implemented in *Turbo machinery* module.

2. Methodology

2.1. Mathematical model

Considering wind flow as an incompressible fluid flow, the governing equations are based on the continuity equation and the momentum equations in unsteady state. The fluctuating velocity components are averaged according to Reynolds Navier–Stokes decomposition (U-RANS) flowing

$$\frac{\partial \rho}{\partial t} + \frac{\partial \rho U_i}{\partial x_i} = 0 \tag{1}$$

$$\rho \frac{\partial U_i}{\partial t} + \rho U_j \frac{\partial U_i}{\partial x_j} = -\frac{\partial \overline{p}}{\partial x_i} + \rho \frac{\partial}{\partial x_j}(\mu \frac{\partial U_i}{\partial x_j} - \overline{u_i' u_j'}) + \rho F \tag{2}$$

F represents external forces (N/kg) added by source term, which is considered zero (F = 0) in the full rotor modelling but represents the action of the blades on the wind flow ($F \neq 0$) through the actuator volume in the hybrid generalized model.

μ is the viscosity and the Reynolds stresses tensor $\overline{u_i' u_j'}$ is written in the Boussinesq formulation as:

$$-\rho \overline{u_i' u_j'} = \mu_t \left(\frac{\partial u_i}{\partial x_j} + \frac{\partial u_j}{\partial x_i} \right) - \frac{2}{3} \rho k \delta_{ij} \tag{3}$$

where δ_{ij} is the Kronecker symbol and μ_t is the dynamics turbulent viscosity. The Reynolds tensor represents an additional parameter that must be taken into account through new equations that requires closure models. Therefore, the k-ε turbulence model with standard and modified coefficient was applied as follows:

- The standard k-ε coefficients given by Launder and Spalding:

$C_\mu = 0.09 \quad C_{\varepsilon 1}=1.44 \quad C_{\varepsilon 2}=1.92 \quad \sigma_k=1.0 \quad \sigma_\varepsilon=1.3$

- The modified constants of Crespo et al. (1985)

$C_\mu = 0.033 \quad C_{\varepsilon 1} = 1.176 \quad C_{\varepsilon 2} = 1.92 \quad \sigma_k = 1.0 \quad \sigma_\varepsilon = 1.3$

2.2. Flow modelling in a rotating frame

The flow modelling in relative motion considers a rotating domain in order to analyse the fluid behaviour through a real moving wind turbine rotor. Thus, the U-RANS equations are resolved near the rotor blade in the moving frame. The repository change related to the angular rotor speed Ω is managed in Code_Saturne 4.0 by the *Turbo-machinery module* where the momentum equations are modified to integrate the acceleration condition that happens because of the benchmark transformation. Therefore, in order to resolve the fluid flow equations in the two referential domains, the rotor is built in a moving frame called the 'Rotor domain' and surrounded by a fixed domain called the 'Stator domain'. The separation between the Rotor/Stator is an interface consisting of delimiting edge cells. The coupling between the domains is ensured in this study, by the flows continuity conservation between different parts. In fact, the flow passage at the interface is managed by the transition *Sliding Meshes* approach that verifies the variable continuity and the flux conservation. This technique considers the interface edge cells as the internal faces joined during calculation at each time steps. The join is performed in Code-Saturne by creating intermediate halo cells [26,27] and the link between the meshes is ensured by the magnitudes with the cells faces in the opposite.

2.3. Flow modelling with a generalized model

Unlike the full rotor simulation, where the geometry of the blade rotor must be represented, the generalized hybrid model consists of replacing the rotor by force acting on the flow thought an actuator model. The basic proposal of the actuator volume is to divide the rotor blades in the radial direction into a number of sections N of annular thickness *dr* as shown in Fig. 1(a). The total force applied to the rotor is the sum of the elementary forces calculated at each angular control volume multiplied by the number of the blades.

The forces acting on a blade element *dr* are a composition of the lift L and drag D forces that are functions of the local angle of attack α, and the local Reynolds number writing as:

$$D = \frac{1}{2}\rho\, U_{rel}^2\, c\,(r/R)\, C_d\,(\alpha, Re) \tag{4}$$

$$L = \frac{1}{2}\rho\, U_{rel}^2\, c\,(r/R)\, C_l\,(\alpha, Re) \tag{5}$$

where C_l and C_d are the lift and drag coefficients respectively, c the blade profile chord and R the span defined by the radius of the circle swept by the blades. The rotation axis is defined by x and the angular speed by Ω. The combination of the incident wind (U_0) and the angular speed give rise to a relative speed (U_{rel}).

The resultant lift and drag forces represent the force that provides the rotor blades with a rotational speed Ω given by:

$$\vec{F} = \vec{L} + \vec{D} \tag{6}$$

Assuming that the rotor has no action on the spanwise flow, the force exerted on a blade element *dr* represented in an orthogonal plane (t, x) illustrated in Fig. 1(b) can be decomposed into two forces as an axial force and a tangential force, defined by Fx and Ft respectively:

$$F_x = B\frac{1}{2\pi r}\frac{\rho c U_{rel}^2}{2}\left(C_L\cos(\phi) + C_D\sin(\phi)\right) \tag{7}$$

$$F_t = B\frac{1}{2\pi r}\frac{\rho c U_{rel}^2}{2}\left(C_L\cos(\phi) - C_D\sin(\phi)\right) \tag{8}$$

The objective of this part is modelling wind turbine rotors with forces acting on wind flow. The actuator volume model is implemented in the transport equations (Eq. (2)) through source term (ρF) in the rotor region previously defined in the computation field. However, the actuator disc concept tends to represent the rotor by a set of elementary surfaces distributed uniformly over a radial element *dr* [11,12,18,19,22]. The elementary surface swept

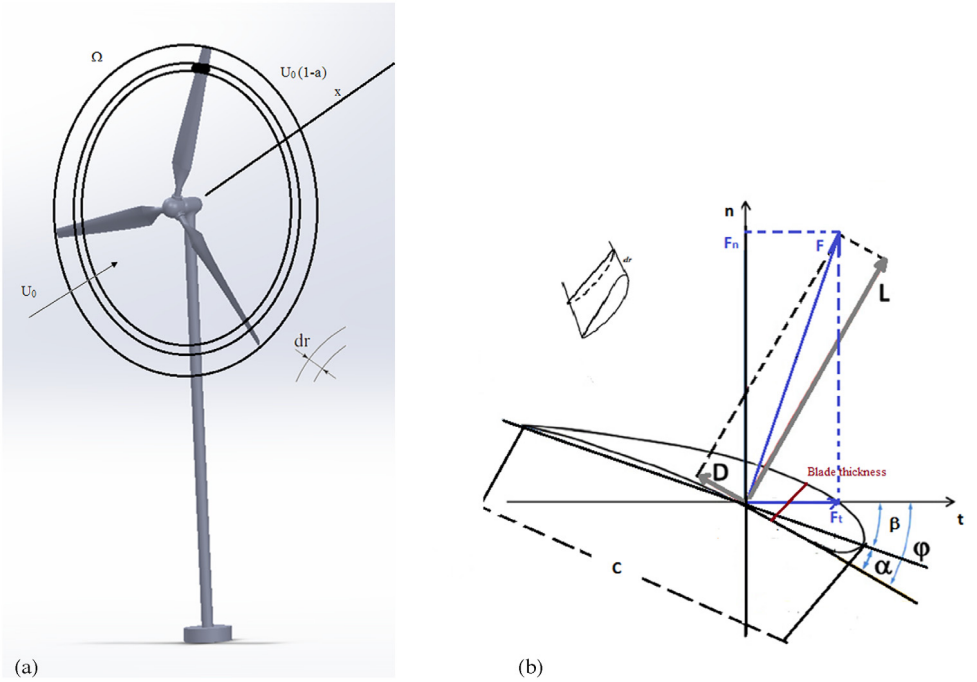

Fig. 1. (a) The rotor discretization in annular volume, (b) the aerodynamic forces applied on a blade element dr.

by the blade element is then defined by $dA = 2\pi r dr$ and the actuator disc surface is relative to $A = \pi R^2$. This implies the source terms integration on an actuator disc of zero thickness. However, according to the finite volume method, the application of the local forces is better controlled within an element volume dv [28,29]. Therefore, we suggest representing the rotor by a disc of diameter equal to the rotor and of a non-zero thickness denoted by ΔX.

The surface forces distribution must then be reduced to a volume distribution by considering annular volumes $dv = 2\pi\ r\Delta x\ dr$. The disc thickness definition is relative to the actual cylindrical volume swept by the rotor [30], that depends mainly on the shape and blades characteristics. M. Jourieh [29] proposed using an actuator disc thickness equal to the product of cord c and sine of the pitch angle. In our case, the real rotor is represented by volume forces distributed on a disc of radius R having a thickness ΔX relative to the blade width and the conicity angle according to the relation:

$$\Delta X = E^*(1 + \sin(\beta)) \tag{9}$$

where E is the blade thickness, determined as a function of the profile chord C and B is the pitch angle.

2.4. Characteristics of the studied turbine

The simulations are performed for the Nibe B 630 kW wind turbine tested by Taylor (1980) [31,32]. The experiments concerned the wake measurements downstream of two wind turbines Nibe A and Nibe B of 40 m diameter. The two turbines spaced by 5D (D is the rotor diameter), were equipped by 4 measuring masts at distances of 2.5D, 4D, 6D and 7.5D. The first mast was equipped with five anemometers and the others with seven anemometers located at different heights. The single wake data averaged over one-minute time were recorded when only the Nibe-B was operational. The records correspond to incident wind speeds ranging from 8.0 m/s to 9.1 m/s measured at hub height with a turbulence intensity ranging from 10 and 15%. The essential characteristics of Nibe B are presented in Table 1.

Table 1. Characteristics of the Nibe B. wind turbine.

Rated power	630 kW
Blade number	3
Rotor diameter, hub height	40 m, 45 m
Cut in, nominal speed, cut out	6, 13, 25 m/s
Angular speed	34 rpm
Twist and pitch angle	11°, 6°
Blade aerofoil	NACA4412/NACA4434

3. Results and discussion

3.1. Full rotor modelling

In order to identify the detailed vortex generated in the wind turbine wake, 3D unsteady simulations of the flow around a moving rotor were initially performed using the Code_Saturne 4.0 [26]. The blade geometries were physically represented in Rotor sub-domain and the U-RANS equations were solved in a fixed and a rotating frame. The transition between the two domains was managed by the sliding interface technique implemented in Code_Saturne 4.0 and the standard k-ε model applied to the turbulence closure.

3.1.1. Geometry

The computational domain is composed of two distinct parts: a moving one representing the 'Rotor' domain and a fixed part, which is the 'Stator' as showed in Fig. 2. The mobile sub-domain or 'Rotor' includes the geometry of the blade based on the NACA4412 profile. However, the Cornering and twisting angles of the blades are not considered in the rotor design and the nacelle is simplified to a disc of 0.1 m that moving with the blade.

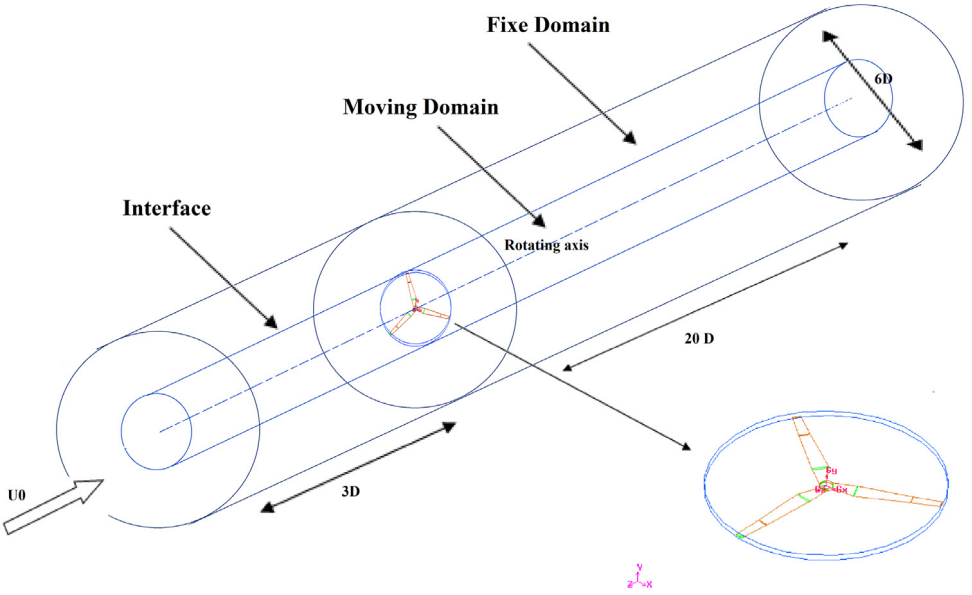

Fig. 2. The Rotor/Stator domain.

The Rotor and Stator are considered as two cylindrical frames in a Cartesian coordinate system whose origin is located at the 'Rotor' centre. A. Abdel Salam et al. [33] have already studied the consideration of the mobile frame border and have introduced a 1D region downstream and upstream of the rotor as a rotational sub-domain. The rest was considered as an inertial frame. However, in relative motion, the transition ('Rotor/Stator') requires the connectivity between neighbouring cell face at the domain limits [25]. For this reason, the consideration of mobile field surrounding only the region close to the rotor introduces additional interfaces, which make the cells homogeneity distribution more difficult to control mainly during the rotation process. In this study, we suggest

Table 2. Comparison of the axial induction factor.

	Number of nodes (10^6)	Experimental induction factor [32]	X/D = 2.5 a = (1−U/U_0)	abs error %
Grid 1	1.9	0.52	0.352	32.3
Grid 2	2.7		0.421	19.03
Grid 3	3.5		0.527	1.34
Grid 4	4.1		0.515	0.96

defining the 'Rotor' as a central cylinder that extends from the inlet to the outlet (Fig. 2) in order to better controls the flow motion between the mobile and the fixed frame. The computational domain boundaries considered by Abdel Salam [33] extended to 25D downstream and 4D in the lateral and transverse directions. The rotor blades were placed at 2D upstream the inlet. C. Carcangiu [34] positioned the rotor at a distance of 5D and used 10D calculation domain in the axial direction and 5D in the transversal direction. In this work the external domain is extended to 23D*6D*6D. The rotor is positioned at 3D downstream of the inlet.

3.1.2. The boundary conditions

A uniform velocity U = 8.5 m/s and a turbulence intensity IT = 11% are imposed to the incident wind speed at the domain inlet and the gradient of (ϕ) is considered zero at the domain exit. On the rotor blade and nacelle, a fluid adhesion condition is applied. In addition, the rotational speed is imposed as a limit condition at the rotor blades.

At the virtual boundaries of the computational domain, the symmetry condition that considers all normal flows on the surface as null is applied.

3.1.3. Grid

Non-uniform hexahedral multi-block grids are built around the mobile Rotor including the three blades geometries shown in Fig. 3. To capture the high shear gradients of the viscous zone, the walls are finely discredited by a boundary layer with a progression ratio of 1.1. In this way, the value of y +, maintained between 150 and 200, remains within the turbulence model limits. To preserve the essential phases of the near wake development, the grid size in longitudinal directions evolves according to an exponential law. However, the objective of this simulation is also to observe the natural flow recovery in the far wake. Thus, we chose to not 'excessively' enlarge the meshes far downstream, to avoid the numerical dissipation of the flow structures. The connectivity between adjacent cells in the limit of the two sub-domains is assured by a particular interface mesh where the same numbers of structured cells are distributed uniformly on both inner and outer the Rotor/Stator limit (Fig. 3(c)).

In order to achieve an independent solution allowing the choice of an adequate discretization, several mesh sizes, ranging from coarse to fine, are tested for a Reynolds number of $Re = 2.3 \times 10^7$. The axial deficit obtained by the different grids is compared with the experimental data in Table 2 within the absolute relative error calculated by:

$$Er = 100\ \frac{\phi i - \phi \exp}{\phi \exp} \tag{10}$$

The simulation results obtained by the grid 3 and grid 4 are the closest to the experimental data. However, the grid 3 of 3.5 million nodes is considered as the optimal grid regarding the more reasonable CPU time. The Rotor and Stator sub-domains are composed of 1.4 and 2.1 million nodes respectively.

3.1.4. Calculation parameters

The simulations are performed for an incident velocity U_0 = 8.54 m/s and a turbulent input intensity It = 11%, corresponding to the experimental case. A rotational speed of 34 rpm is imposed on the rotor sub-domain. The time step is set at $\delta t = 0.003$ s corresponding to a rotor displacement of $\theta = 0.6120$. This time step is selected according to the smallest cell size where ($\Omega \delta t \leqslant \delta x$) allowing thus the interface flows conservation and ensuring the smooth operation of the *Sliding Mesh* model. The simulations are carried out for a total time of 120 s necessary for tracking a wind particle in the wake. It corresponds to 68 wind turbine rotation cycles.

Using 20 Xeon 2.50 GHz processors, the simulations ran on a cumulative computation time of 305 h (12.73 days). The wake data obtained correspond to a rotor displacement of 61.2°.

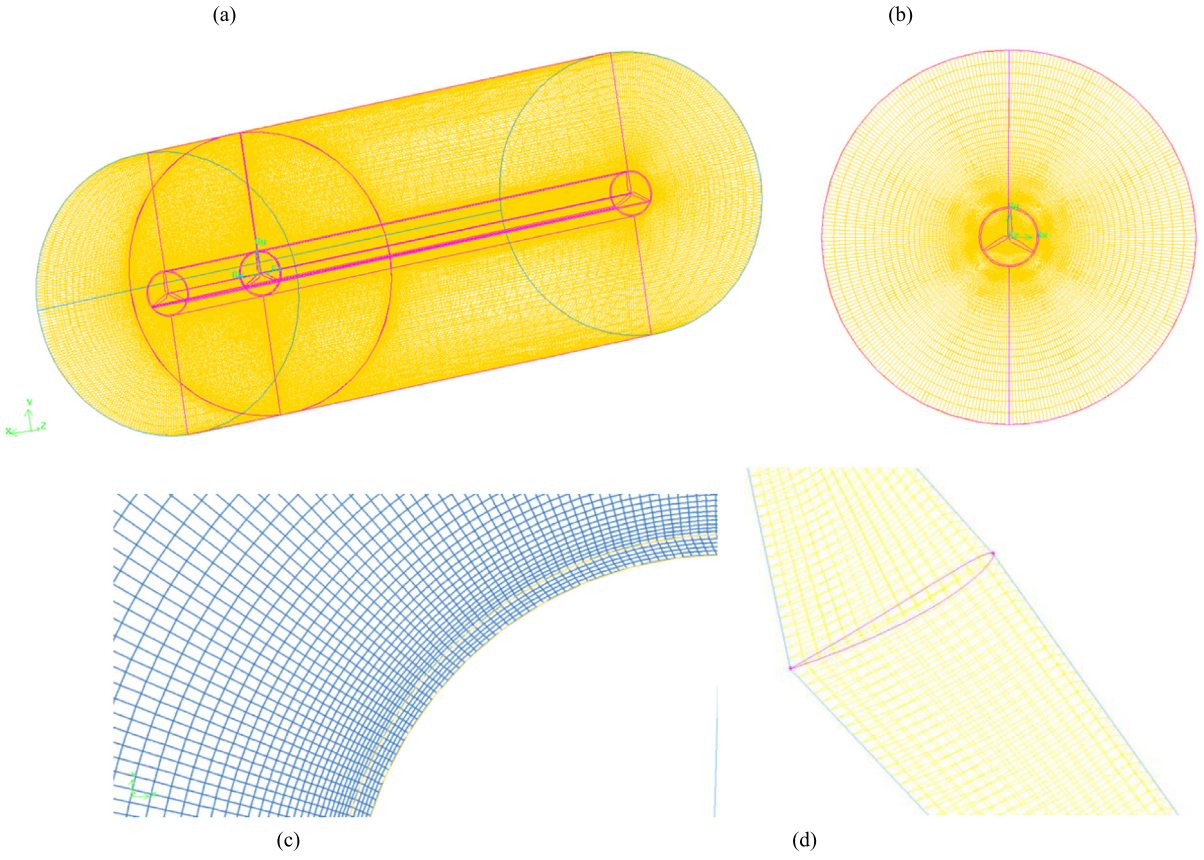

Fig. 3. The domain computation grid (a); front plan (b); typical configuration of the mesh at the interface (c); mesh on the blade surface (d).

3.1.5. Velocity profiles of the full rotor modelling

The speed profiles in the wake are normalized with respect to the input speed by U/U_0 and are averaged over time in order to allow comparison with the experimental data.

The averaged velocity deficit are plotted in Fig. 4 at the position of X = 2.5D, X = 4D, X = 6D and X = 7.5D. In the near wake region at the position X = 2.5D, the instantaneous velocity decrease progressively to reach a minimum varying between 0.37 and 0.5. It is noted that the time required for the air particles passing through the rotor to reach the first measuring mast is about 11.75 s. During this period, the rotor would have completed 6.5 rotation cycles. Subsequently, the airflow affected by the speed deficit gradually reaches the downstream flow. A gradual speed recovery is noted in the far wake at a distance of X = 7.5D, where a ratio of 80% of the reference speed is recorded. The comparison between the average normalized speeds and the measured data show a good agreement between the simulation results and the Taylor records [32].

For the second mast at X = 4D, the width of the wake corresponds to the experimental data, but the minimum simulation speed deficit reports an overestimation of about 20%. This can be translated by the position of mast 2 which is located at a close distance of 1D downstream the Nibe A turbine. In fact, even if this later is stopped, the recordings of the second mast are affected by the nacelle and the tower of the turbine A [32].

At the distances corresponding to the position of the masts 3 and 4, the simulations results are in adequacy with the experimental data. However, the average axial velocity calculated over the entire simulation time shows a slight overestimation of the speed deficit in the far wake.

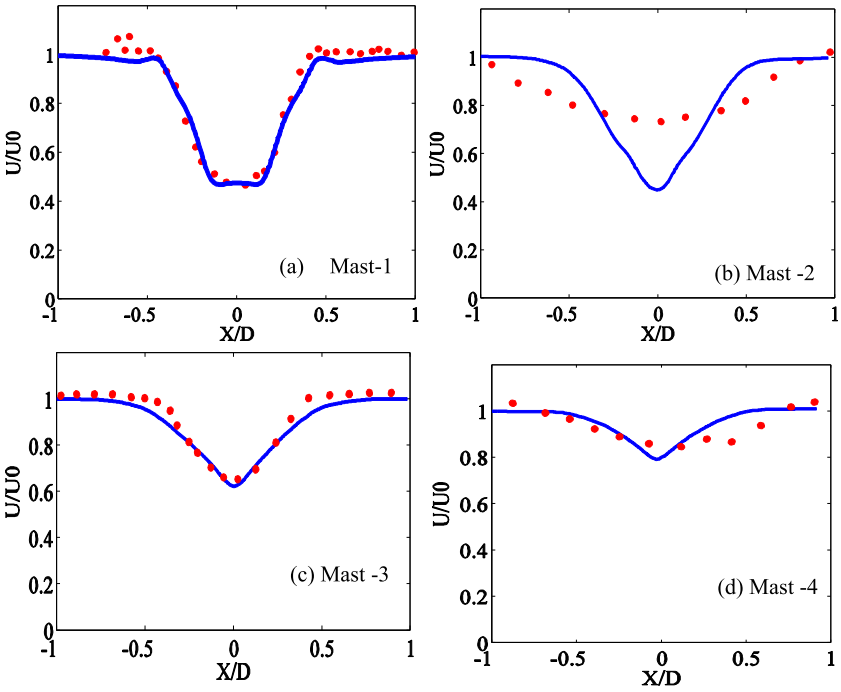

Fig. 4. The averaged velocity profile at the positions (a) X = 2.5D (b) X = 4D (C) X = 6D and (d) X = 7.5D downstream rotor; for $U_0 = 8.5$ m/s and I = 11%.

3.1.6. The turbulence intensity

The turbulence intensity is evaluated according to the turbulent kinetic energy normalized by the free flow velocity according to the following equation:

$$I_u = \frac{1}{U_0}\sqrt{\frac{2}{3}k}. \tag{11}$$

The turbulence intensity profiles recorded at different positions in the wake of the rotor are compared with experimental data in Fig. 5. The results corresponding to the position X = 2.5D (Mast-1) show a double peak of the turbulence intensity recorded at the ends of the rotor. This is due to the swirling detachment induced by the tips blades rotation. In the wake centre, the turbulence intensity is rather low and the flow is strongly influenced by the rotor dimensions.

In the far wake, represented by the masts 3 and 4, the measured values show a gradual attenuation of the turbulence intensity from X = 6D, while the peaks are maintained in the simulations up to the distance X = 7D. In addition, a variation in turbulence intensity ranging from 2 to 10% compared to experimental measurements is also observed in the wake. The possible causes of this difference may be related to (i) the effects of atmospheric stability affecting measured values [35] or (ii) to uncertainties in the measurement of undisturbed turbulent intensity [32,36]. Indeed, due to the absence of upstream measurements, the undisturbed turbulence intensity was estimated from an anemometer placed at a height of 3 m on the Mast-1 [32,37]. Otherwise, the difference in the turbulence intensity can also be related to the k-ε standard model ability to represent the zones of strong gradients generated by the blades rotation. According to [25,30,37,38], the use of low Reynolds number models or the LES to respond to the turbulence anisotropy in the wake can answer this deficiency.

3.1.7. The wake streamlines

The results management in the wake in the unsteady calculation remains subjective because of the fluid particle position at each time step. The Fig. 6 depicted the streamline at different times t for Reynolds number $Re = 2.3 \times 10^7$ and rotation speed of $\Omega = 3.5$ rad/s. After 3 cycles of rotation, corresponding to the moment

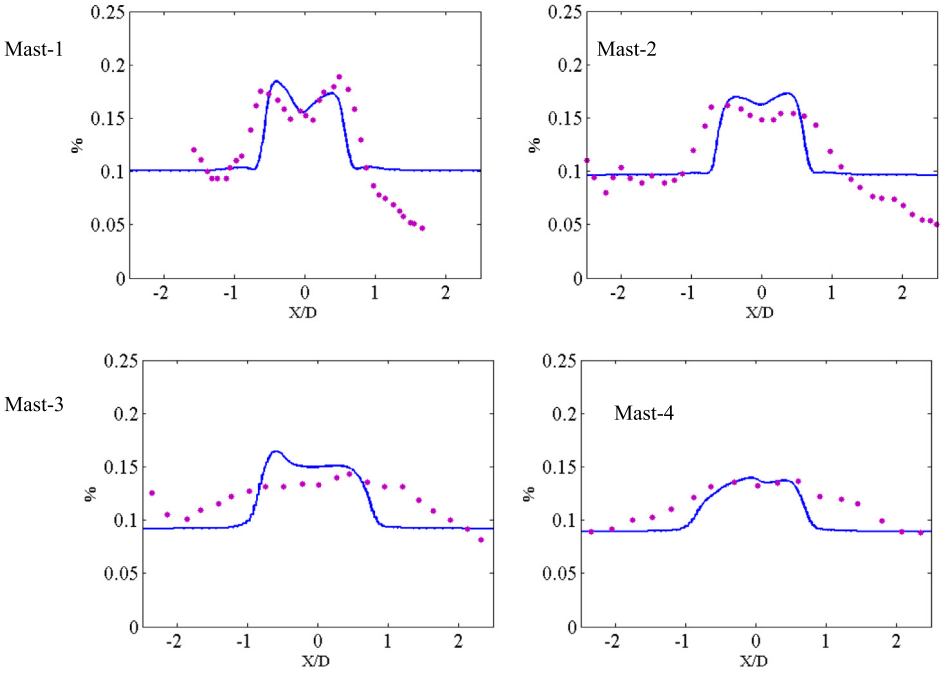

Fig. 5. Turbulence intensity profiles in the wake of Nibe B compared to Taylor records [32] for different mast positions.

t = 7.8 s, the results highlight the formation of two structured and symmetrical recirculation zones immediately downstream of the rotor. They are a priori due to the displacement of vortex structures resulting from the dynamic stall on the blades [12].

The displacement of these wind particles in such rotational movement causes a three-dimensional torsion of the downstream flow. In accordance with the description of B. Sanderse [2], the two symmetrical and counter-rotating vortices are mainly delimited by the streamlines passing through the ends of the blades. They become more and more pronounced and reach a form of maximum structuring at t = 15 s. Note that the progressive generation of these two vortices at the immediate rotor downstream is not commonly detectable by the average calculation [23].

These two vortices are progressively stretched and moved downstream. Their continual elongations cause their gradual deterioration at t = 24 s.

Between t = 30 s and t = 48 s, we observe the beginning of the constitution of one same shear zone, giving rise to a large vortex which wraps around its rotation axis. The global wake formation stabilizes from time t = 50 s, to approach an elliptical shape spreading up to 3D. These results are similar to those reported by Vermeer [6] defining the near wake as the immediate downstream region, between the rotor position and a distance of $0 < X < 3D$.

The full plane of Fig. 6 shows that the end of the near wake zone interacts in a very complex way with the surrounding environment. In fact, at the position around X = 7.5D, a sinusoidal detachment of small swirling vortex are prolonged in the flow direction distinguishing the transition region to the far wake. Note that this sinusoidal flow oscillation caused by the detachment of regular vortices produce the wake meandering which is the subject of various investigations [39]. Beyond X > 10D, the detached vortices merge into the surrounding environment to join the fully developed flow.

3.1.8. The three-dimensional wake

The three-dimensional evolution of the flow field in the near-rotor region is analysed by plotting the iso-velocity surface illustrated in Fig. 7, for four instants as t = 21 s, t = 60.3 s, t = 78.3 s, and t = 111.3 s. The progress parameter defined by $\lambda = \omega R/U_0$ is about $\lambda = 8.23$ and a turbulence rate of 11%.

This post-processing results provides access to very interesting information on wake physics. One can see that the small isolated vortices generated at the tip blades are dragged in the wake by the local wind flow. However,

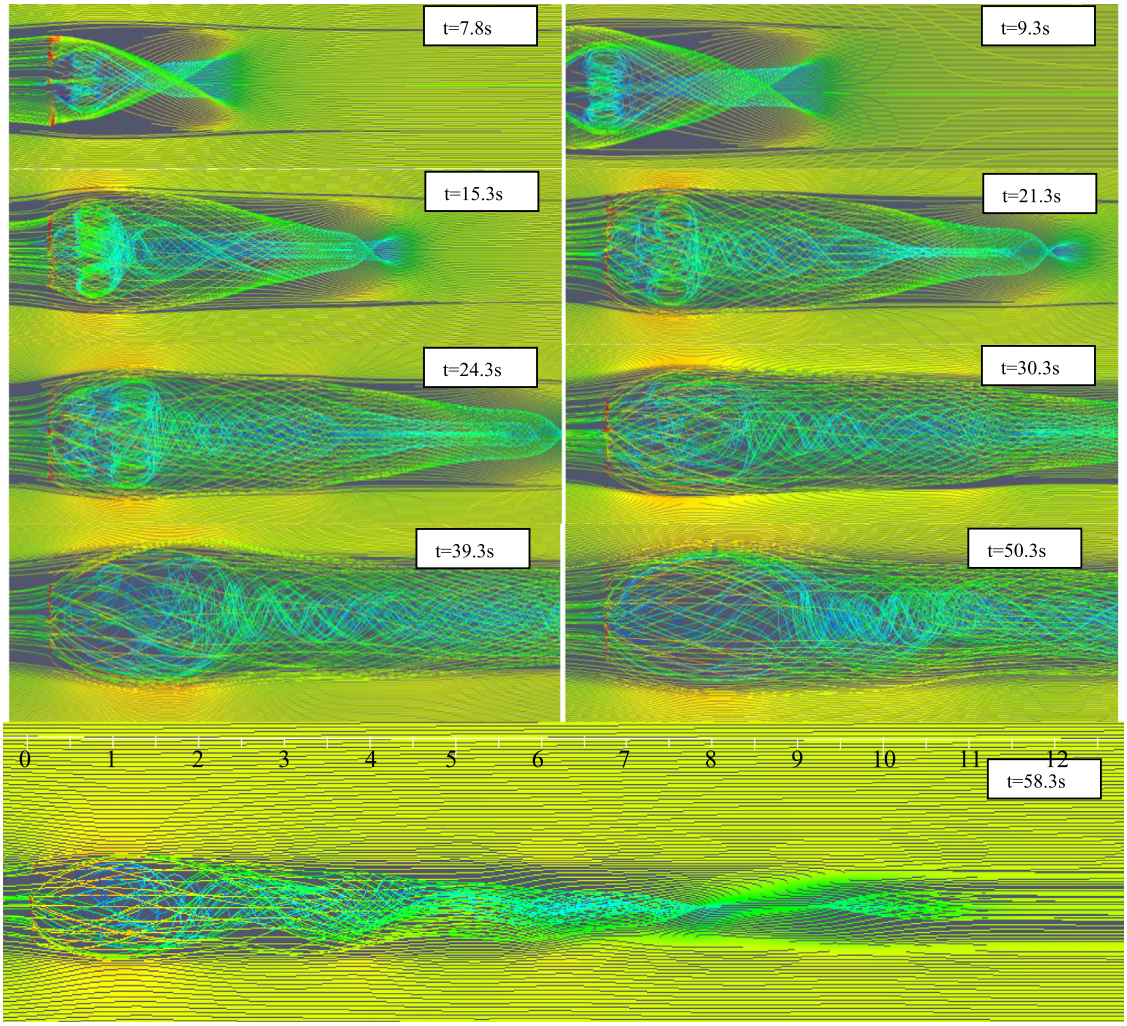

Fig. 6. Spatial and temporal evolution of streamlines on the central plane: the first eight planes give a zoom on the near wake and the last the overall wake.

since the blades are moving in a circular orbit, but under an axial wind flow, the blade tip vortices are displaced to the rotor downstream in a helical path. At t = 21 s, the vortices appear initially as a separate spiral in the rotor zone and are progressively transported downstream by the angular velocity. After, at t = 60 s, the distance between the vortices widens to gradually merge into the wake among a distance of 0.5D. The dissipation of these marginal vortices creates a velocity separation layer, which delimits the inner wake zone of the external ambient environment. Various RANS study using different turbulence models such as SST-Kw [25] and Spalart-Allmaras [34] have also distinguished a decay distance of marginal vortices similar to 0.5D. However, the experimental works have shown that the mechanism of marginal vortices formation is maintained to a distance of 1.2D [29] and their dissipation depends on the turbulence rate of the surrounding environment [39] and on a progress parameter λ.

Fig. 8 gives a three-dimensional view of the wake expansion in the flow direction. It clearly shows the formation of an area encompassing a region of low speed. It is similar to a tubular shape that wraps around its axis of rotation. At the end of this zone, we observe the vortex structure detachment in the far wake.

As main results, the full rotor simulations give important information on the single wake but seem more complex to perform for wind farm composed of numerous neighbouring wind turbines. In fact, the adjacent cells connectivity optimization at the relative motion frames remains strongly difficult within the variable interpolation at the Rotor/Stator interface. Note that the *Sliding Mesh* technique in Code_Saturne considers additional halo cells at the interface

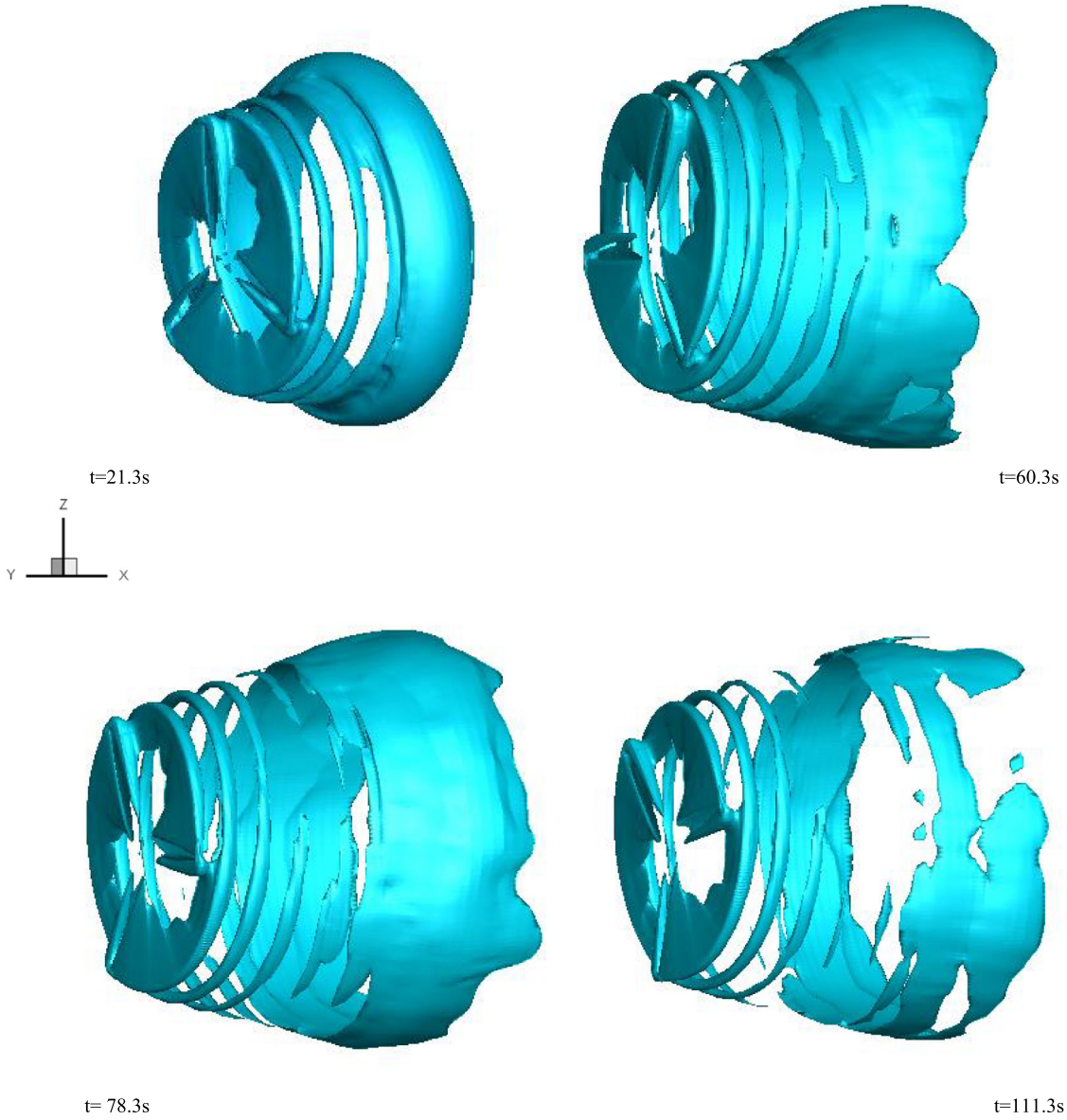

Fig. 7. Unsteady evolutions of the wake development by the iso-velocity surface (D = 40 m, U_0 = 8.5 m/s, I = 11%, λ = 8.23); k-ε model.

that must be in perfect distribution to grantee the variable continuity. For this reason, even if it is possible to perform for single or twice full rotors the control of several ones remains inaccessible today.

3.2. The generalized wake model

The direct simulations around the full rotor proved to be expensive for the wake effects assessment in a wind farm. Imperatively, hybrid solutions are alternatives to direct simulation. Therefore, a generalized actuator volume model (D-VA) is developed in this second part. It consists of representing the real rotor by the force acting on the wind flow by an actuator disc with no zero thickness, without considering a supplement dissipation rate. The external forces are implemented to the Navier Stokes' equations through additional source terms in explicit and implicit formulation. The equations are resolved in a turbulent steady state in an inertial domain by a RANS formulation. The modified

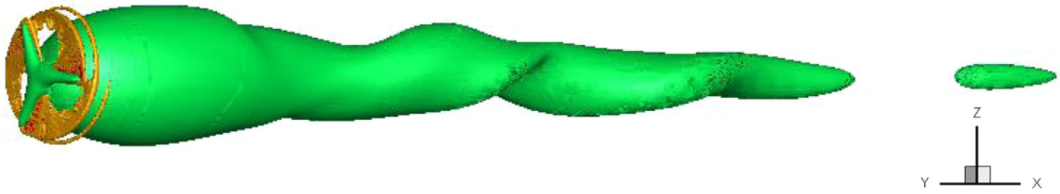

Fig. 8. The wake expansion at t = 60.3 s.

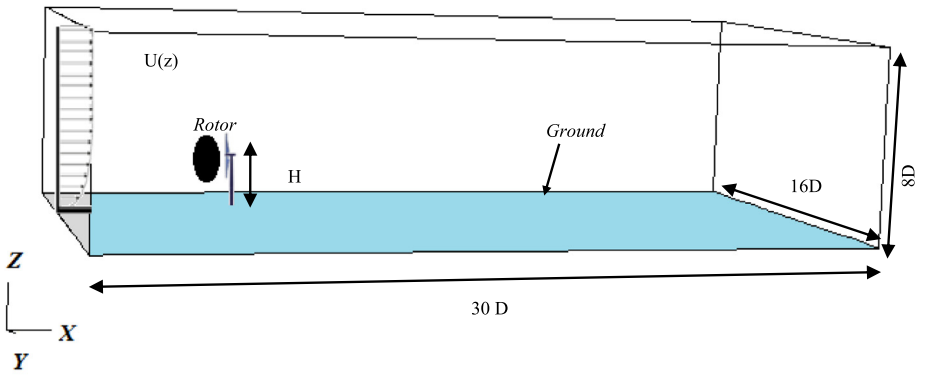

Fig. 9. Calculation domain.

k-ε for neutral atmospheric boundary layer flows is applied to close the turbulence model where ($C_\mu = 0.033$, $C_{\varepsilon 1} = 1.176$, $C_{\varepsilon 2} = 1.92$, $\sigma_k = 1.0$ and $\sigma_\varepsilon = 1.3$). The ability of the generalized actuator volume model to represent the wake is demonstrated by series of validations with experimental data. Indeed, the wake prediction using the generalized hybrid model are carried out for different wind turbines, as the Nibe B 630 kW turbine, presented in full rotor simulation [31,32], and the Danwin 180 kW experimental wind turbine, operating at a rotation speed of 42 rpm, with a rotor diameter D = 23 m and a hub height of H = 31 m [40]. These databases have often been used for numerical wake models validation [14,18,20,22,33]. However, it should be noted that only velocity deficit and turbulent intensity measurements at different positions in the wake are available. The aerodynamic characteristics details that are of industrial interest are unfortunately confidential. Therefore, the development of the proposed hybrid models is essentially based on the turbine thrust data and power coefficients provided by the manufacturer.

3.2.1. Geometric parameters

Unlike the complete simulations where the rotor is represented by its exact geometry, in this component, the effects of the rotor on the flow are represented by aerodynamic forces distributed over an actuator volume of dimension equivalent to the rotor. It is therefore no longer necessary to separate the domain of the rotor from the surrounding environment. The geometric parameters for evaluating wake behaviour are described in Fig. 9. The external domain is built around the rotor in a parallelepiped considering only the rotor diameter D and the hub height H. The external domain are located at optimum distances of (30D × 16D × 8D). The rotor is positioned at 6 D from the inlet boundary and the ground is characterized by a roughness value $z_0 = 0.01$ m.

3.2.2. The boundary conditions

In summary, the applied boundary conditions are

- On the ground: an adhesion condition is applied where the velocity components are zero and the roughness value is $z_0 = 0.01$.
- At the domain exit, the gradients (ϕ) are zero.
- At the upper domain boundary, the symmetry condition which considers all normal flows on the surface as null is applied.

Table 3. Grid tests.

	Cell number	Rotor node number	Node/ rotor diameter	X/D = 2.5 a = (1−U/U$_0$)	Error relative %	X/D = 6 a = (1−U/U$_0$)	Error relative %
Grid 1	138 679	176	3/D	0.640	23.17	0.400	42.35
Grid 2	647 038	330	4/D	0.543	4.42	0.341	20.99
Grid 3	784 559	800	5/D	0.510	1.92	0.292	6.91
Grid 4	1 353 336	800	8/D	0.512	1.53	0.290	3.20
Grid 5	1 924 241	800	12/D	0.510	1.50	0.280	–

- To simulate a wind turbine in the atmospheric boundary layer, at the inlet the logarithmic velocity profile is considered, along with the turbulent kinetic energy profile k (z) and the evolution the dissipation rate ε (z) given respectively by:

$$\overline{u}(z) = \left(\frac{u_*}{\kappa}\right)\left(\ln\frac{z}{z_0}\right) \tag{12}$$

$$k(z) = 5.48u_*^2 \tag{13}$$

$$\varepsilon(z) = \frac{u_*^3}{\kappa\, z} \tag{14}$$

z is the turbine height and z_0 the roughness length. The constant 5.48 is a value experimentally determined. κ is the Von Karman constant $\kappa = 0.42$ and u^* is the friction velocity.

3.2.3. Grid

Even if in the hybrid model, the rotor region does not require the blades geometry representation, the near wake being the seat of strong speed gradients, also requires a fine discretization for a certain distance downstream. In accordance with M.P. Laan et al. [35] study, several tests are performed in this paper, considering 4, 8 and 12 nodes per rotor diameter over a minimum region of 10D behind the rotor. This avoids a numeric diffusion caused by the abrupt passage of fine meshes towards too large meshes in the far wake. In other hands, note that in most hybrid methods, the actuator disc thickness was generally considered zero [12,22,41]. Here, we apply the hybrid models to actuator volumes discretized by a single mesh in the direction of flow. The length of this cell representing the rotor thickness (ΔX) is defined according to the radius R, the cord c and the angle of attack B.

For that, a parametric study is carried out for four-disc thicknesses chosen according to Eq. (9) (ΔX = E (1+ sin (B))) where E is the thickness of the blade determined according to the cord of the profile.

Having little information on the blade geometry, we considered different values of the average cord as c = 7.5%, 9%, 16% and 20% of the blade span corresponding to the different volume thicknesses ΔX1, ΔX2, ΔX3 and ΔX4. The speed deficits obtained in the wake as a function of the actuator volume thickness are compared with the experimental data of the Nibe 630 kW [32]. Note that, the greatest results were obtained by ΔX3 and ΔX4 thickness.

The sensitivity tests to the computation domain discretization are carried out for Nibe B (U_0 = 8.54 m/s and Ct = 0.82). Thus, five grids that are distinguished mainly by the total size meshes and the rotor region grid density are tested. The axial induction factor calculated with the relation (a = 1 − U/U^0) is compared with the experimental records in the near and far wake at X = 2.5 D and X = 6D respectively.

The Table 3 shows the deficit and the relative error recorded for each grid. Note that despite the large dimensions of the computational domain (exceeding 30 D in the flow direction), acceptable velocity deficit results are obtained near X = 2.5D with low node numbers. The test on the nodes number by rotor diameter confirmed that mesh refinement by 8noued/D and 12noued/D downstream the rotor in a region up to 10 D, allows improving the far wake result accordingly to the recommendations provided by [35].

The mesh retained for the Nibe B calculations corresponds to the grid 4 composed of 1.353.336 structured and non-uniform rectangular cells within 8 nodes per rotor diameter. The rotor disc is meshed in (O) with 800 control volumes. At ground level, the value of y + is maintained between 50 and 150.

Table 4. Principal simulations parameters of Nibe B 630 kW.

D [m]	H [m]	z_0 [m]	CT [–]	U_0 [m/s]	IT %	Mast positions
			0.82	8.54	11	
40	45	0.01	0.77	9.56	11	2.5D–4D–6D–7.5D
			0.67	11.52	10.5	

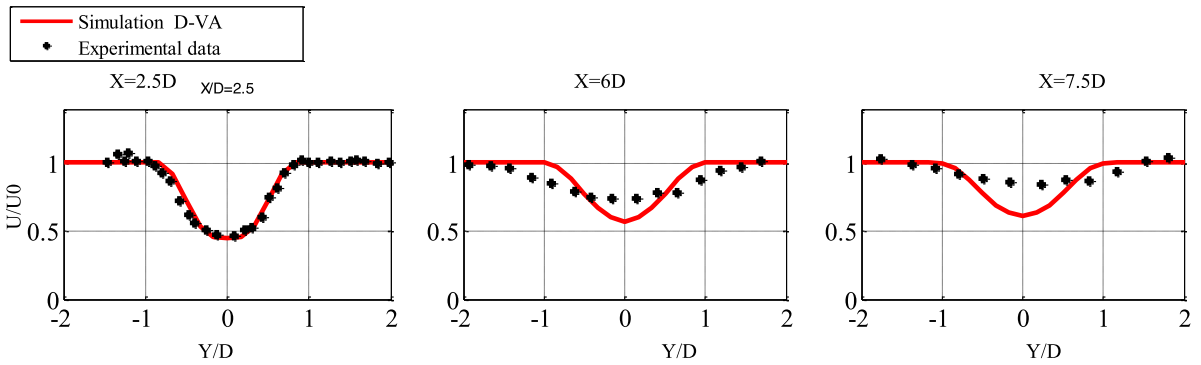

Fig. 10. The radial velocity deficit downstream of the Nibe B (Ct = 0.82 and U_0 = 8.54 m/s). (For interpretation of the references to colour in this figure legend, the reader is referred to the web version of this article.)

3.2.4. Generalized volume applied to the Nibe B wind turbine

The simulations around the Nibe B 630 kW turbine are performed for three reference velocity values, namely U_0 = 8.54 m/s, U_0 = 9.56 m/s and U_0 = 11.52 m/s corresponding to the thrust coefficient of Ct = 0.82, Ct = 0.77 and Ct = 0.67 respectively. In accordance with Taylor's experimental conditions [32] the turbine is placed on a homogeneous ground with a soil roughness z_0 = 0.01 m. The main characteristics considered in the simulations are summarized in Table 4.

The wake results obtained from the generalized actuator volume model (D-VA) (in explicit formulation) using the modified k-ε model ($C\mu = 0.033$ and $C\varepsilon 1 = 1.176$) are compared with the experimental data in Figs. 10–12. They represent the average radial distribution of the speed deficit normalized by the considered incident velocities (U/U_0) for 8.54 m/s, 9.56 m/s, and 11.52 m/s. The results are plotted at Mast 1, Mast 3 and Mast 4 positioned at distances X = 2.5D, X = 6D and X = 7.5D respectively. Due to the lower quality of the Mast 2 record at X = 4D [32] the corresponding result are not presented here.

We note, from the different figures that the results obtained with the proposed model are in good agreement with the Taylor records and that for all incident velocities U_0 and each mast position. Indeed, one can see a close correspondence of the normalized velocity deficit manly in the near wake corresponding to X = 2.5D (figures on the left). Note that, usually, the actuator disc models of zero thickness applied without any modification in dissipation rate as the Crespo model [41] tend to underestimate the velocity deficit and fail to reproduce the wake principally in close rotor region. Hence, the most developed model looked for improving the near wake prediction [16–29]. The results obtained in this paper demonstrate the ability of the proposed generalized volume model D-VA to reproduce the flow properties behind the rotor. Indeed, the present simulations give particularly interesting results at the critical position of the Mast 1 (X = 2.5D). In harmony with the measured data [32], the speed deficit achieves a maximum decrease of the initial speed of about $U/U_0 = 0.48$ with (U_0 = 8.54 m/s and Ct = 0.82). The relative error between the simulations and the recordings varies around 1.5%. A good concordance is also observed in the near wake for (U_0 = 9.56 m/s and Ct = 0.77) and (U_0 = 11.52 m/s and Ct = 0.67).

However, it is noted that the far wake rehabilitation is reached more quickly by the experimental data. In fact, an overestimate of the axial deficit of about 5% is recorded at Mast 4 corresponding to 7.5D. It should be noted that this overestimation was also observed in the full rotor simulations. This far region is characterized by the convective mixing of the disturbed atmospheric flow that participates in the rapid rehabilitation of the wake.

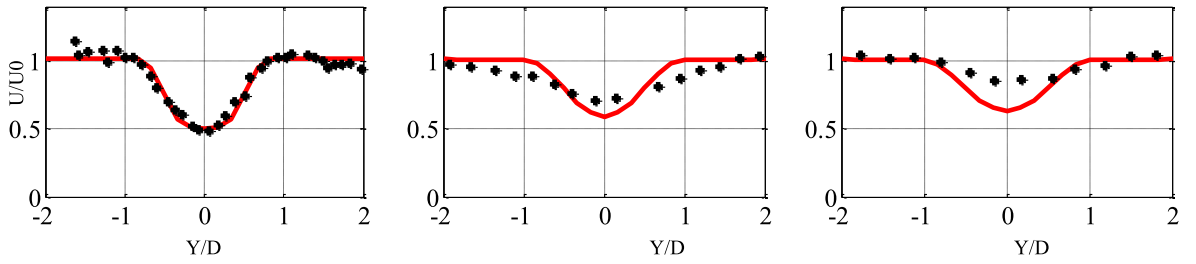

Fig. 11. The radial velocity deficit downstream of the Nibe B (Ct = 0.77 and U_0 = 9.56 m/s). (For interpretation of the references to colour in this figure legend, the reader is referred to the web version of this article.)

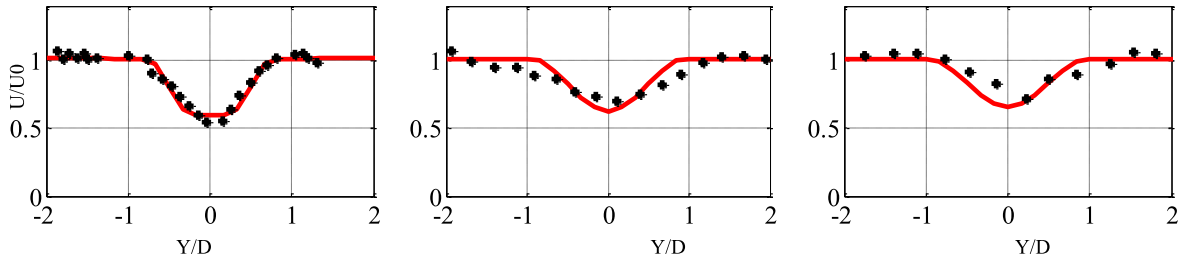

Fig. 12. The radial velocity deficit downstream of the Nibe B (Ct = 0.67 and U_0 = 11.52 m/s). (For interpretation of the references to colour in this figure legend, the reader is referred to the web version of this article.)

Table 5. The main characteristic of the Danwin 180 kW simulations.

D [m]	H [m]	z_0 [m]	CT [–]	U_0 [m/s]	IT %	Position des mats
						Mast 1 = 1D
		0.01				Mast 2 = 4.15D
23	30		0.82	8	7	Mast 3 = 9.4Dl

3.2.5. Generalized volume applied to the Danwin 180 kw

The Danwin 180 kW experimental wind turbine is a three-bladed wind turbine with a rotation speed of 42 rpm and a diameter of D = 23 m at a hub height of H = 30 m (Table 5). The blade profile belongs to the NACA632xx series with relative thicknesses that vary between 12% and 32% [18]. The angle of the blades conicity with the vertical is zero. The simulations are performed for a wind speed U_0 = 8 m/s defined at the hub height. Variations in incident velocity U (z), turbulent energy k (z), and dissipation ε (z) are imposed as input conditions in the same way as for Nibe B.

Fig. 13 presents the comparisons between the speed deficit curve determined using the D-VA model and the experimental measurements of Magnusson et al. (1996) [40]. We note a very good agreement between the experimental data and the D-VA model that successfully reproduce the wake in the near and far regions. In fact, the relative error in the two regions, in this case, is very low, especially for the distant wake X = 4.15D and X = 9 D.

3.2.6. Implicit or explicit implementation of the generalized (D-VA) model

The accuracy of the proposed model depends mainly on the manner to introduce the source term in the flow field production in the iterative process and on the consideration of physical flow properties stored at the geometric control volume centre at the rotor region. In fact, the results of Figs. 10–13 are obtained using an explicit implementation of the source term in the Navier stokes equation. However, in the finite volume method used, the source term linearization given by Patankar [28] assumes that the additional external forces should be implemented through an explicit and/or an implicit formulation as $((S_T)_\phi = (S_T)_C + (S_T)_p\phi)$ (with $((S_T)_C$ is the explicit term and $(S_T)_p$ is the implicit term). This allows to implicitly introducing the actuator volume model (D-VA) as a flow velocity function within $(S_T)_C = 0$ and $(S_T)_p \neq 0$ or assuming that the physical properties of the flow are constant throughout the rotor

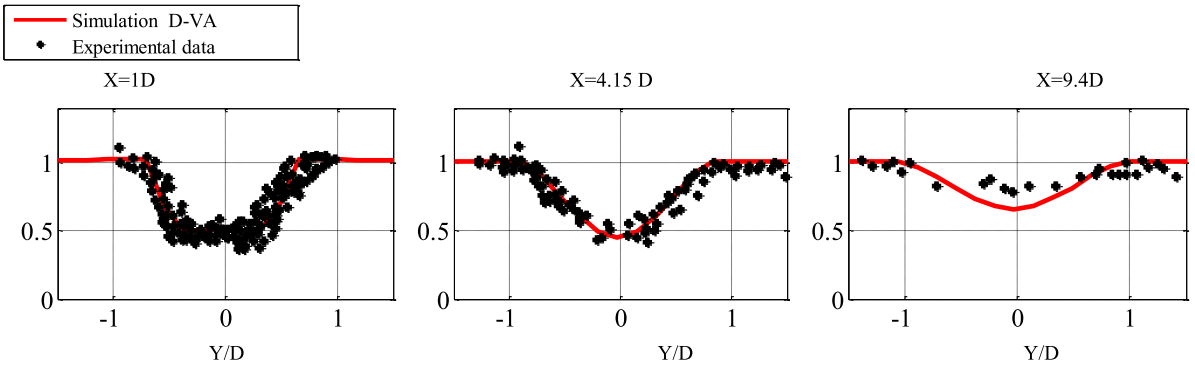

Fig. 13. The radial velocity deficit downstream the Danwin 180 kW; Ct = 0.82 and U_0 = 8 m/s. (For interpretation of the references to colour in this figure legend, the reader is referred to the web version of this article.)

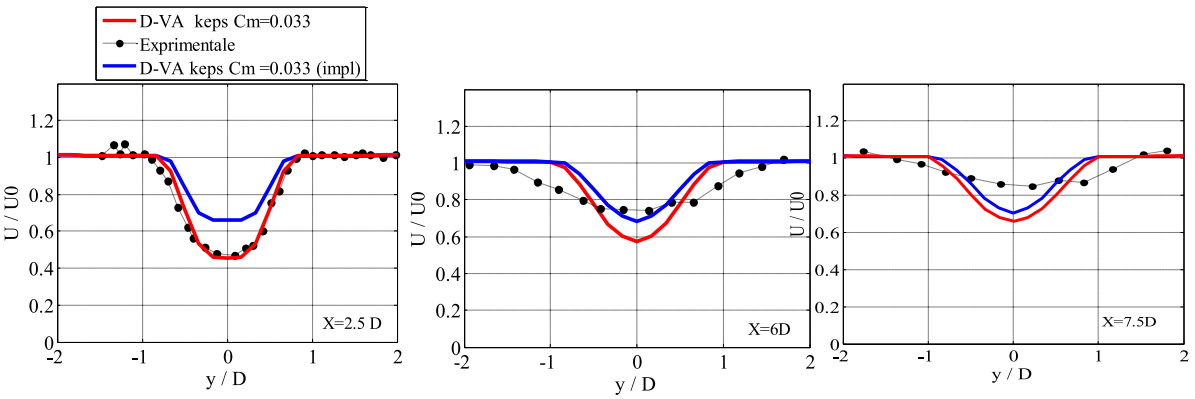

Fig. 14. The velocity deficit with explicit and implicit actuator volume—Nibe 630 kW; Ct = 0.82 and U_0 = 8.54 m/s. (For interpretation of the references to colour in this figure legend, the reader is referred to the web version of this article.)

control volume and the D-VA model is then introduced explicitly by $(ST)_C \neq 0$ and $(ST)p = 0$. In order to analyses how these two formulations affect the wake behaviour in the flow field, the D-VA model is implemented in both explicit and implicit source term and the results are compared to the experimental data. Note that the explicit term in the momentum equation is (kg m/s^2) and the implicit term is (kg/s). An adjustment is therefore necessary in the implicit case. Masson et al. [17] proposed to normalize the source term by the local velocity obtained at the previous iteration or more simply by the reference velocity U_0.

Figs. 14 and 15 represent the normalized axial velocity deficit reproduced by the two approaches downstream of the Nibe 630 kW turbine (for U_0 = 8.5 m/s and Ct = 0.82) and the Danwin 180 kW wind turbine. As previously shown in Figs. 10–13, the results obtained by the actuator volume in the explicit formulation (in red) give a better correlation with the experimental recordings for the two turbines in particular in the near wake at X = 2.5D for the Nibe B and X = 1D and X = 4D downstream of the Danwin 180 kW.

The implicit formulation of the D-VA model shows a significant underestimation of the speed decrease in the wake region and the deficit obtained does not exceed 70% when the experimental values and the explicit formulation are close to 50% of U_0. These results are in line with the Crespo preliminary wake analysis [42], nevertheless more recent studies based on the CDF-actuator disc models (with zero thickness) have shown that the implicit formulation makes it possible to better manage the flow in the vicinity of the rotor, but requires the introduction of more sophisticated technique for calculating the forces [43,44]. In fact, to improve the near wake prediction, Réthoré and Sørensen [44,45] have developed a BEM-CFD model to implicitly evaluate the forces applied on an actuator disc of zero thickness. Hussein et al. [43] and Markidis et al. [14] used the VBM model, to improve the wake results of the Tjaereborg-2MW turbine and Nibe 630 kW respectively.

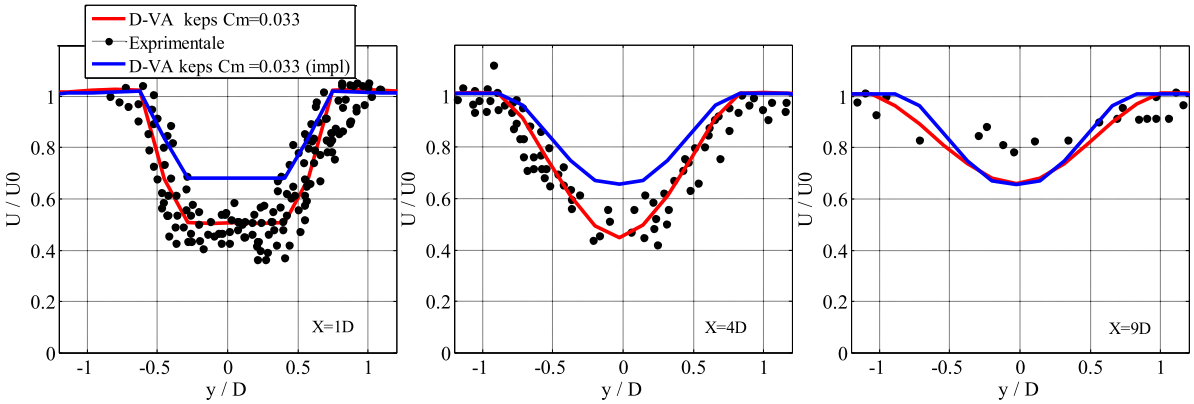

Fig. 15. The velocity deficit with explicit and implicit actuator volume—Danwin 180 kW; Ct = 0.82 and $U_0 = 8$ m/s.

According to Masson et al. [17] and Mikkelsen [12] studies, the explicit formulation allows an easier implementation of the actuator disc model but can introduce the numerical oscillation results. Mikkelsen [12] pointed out that a more or less fine discretization of the rotor makes it possible to avoid the solution oscillations, which can occur during the integration of the forces on a disc of zero thickness. Note that, in this study, no divergence or solution oscillations were observed in the force implementation on the volume disc in the explicit or implicit application of the D-VA model. We assume that it is thanks to the disc thickness that gives more numerical stability at the level of the rotor region.

3.2.7. Comparison with the El Kasmi and Masson model

To improve the actuator disc model, A. El Kasmi and C. Masson [22] proposed an extended k-ε model based on the work of Chen and Kim [46]. It consists in adding a term in the dissipation equation of the turbulent kinetic energy ε, to improve the dissipation proportionally to the turbulence production Pκ. The proposed relation was $S_\varepsilon = C_{\varepsilon 4} P^2 \kappa / \rho k$ with a dissipation parameter of $C_{\varepsilon 4} = 0.37$. This modification was introduced into a cylindrical region of e = ±0.25D which surrounds the rotor. The El Kasmi and Masson actuator model was implemented on a disc with zero thickness in an axisymmetric formulation in Fluent code to predict the wake of the Nibe 630 kW, the Danwin 180 kW and the MOD-0A 100 kW turbine. These authors obtained a very good concordance during the confrontation with the experimental results. In this paper, the D-VA rotor model is applied in a three-dimensional domain to an actuator volume (D-VA) with no additional term in the dissipation rate equation. The rotor thickness (ΔX) is evaluated according to the radius R, the cord c and the angle of attack B. The D-VA results obtained with (ΔX3) are compared in Fig. 16 with those of El Kasmi [22] and Crespo [41] and Taylor measurements [32], for a turbulence intensity of 11% and different values of Ct = 0.67; 0.77 and 0.82.

The figure shows that the wake behaviour established by the present D-VA model is in perfect harmony with the results of El Kasmi [22], and this, for the different values of Ct. = 2.5D and X = 6D, the velocity profiles of the near and far wake area coincide very well. The estimated relative error between the two approaches is less than 1.5%. The delay in the natural recovery of speed recorded in the far wake by the D-VA model is also observed with the El Kasmi model [22]. However, the soil effects in our model are felt by a slight extension of the wake observed at X = 7.5D. It showed by the descent of the wake zone due to the soil attraction. The wake prediction of the proposed model is significantly improved in comparison with the Crespo approach [41] that gives results almost similar to the implicit formulation presented in the previous section.

The difference between the present D-VA and El Kasmi and Masson models resides in the dissipation rate increase in the extended k-ε model by the increase of the dissipation constant Cε4. This term represents the role of the transfer rate of turbulent energy from large scales to small-scale turbulence downstream the turbine. Therefore, the wake rotor reproduction, in this case, is very sensitive to the consideration of the kinetic energy lost by the fluid and transformed into turbulent energy. Indeed, the application of an actuator disc model on a very thin surface acts as a singularity in a fluid flow that induces significant kinetic energy levels [17]. While an increase in turbulent intensity promotes mixing and leads to a faster return of speed in the wake [12,18,44]. This is generally the case

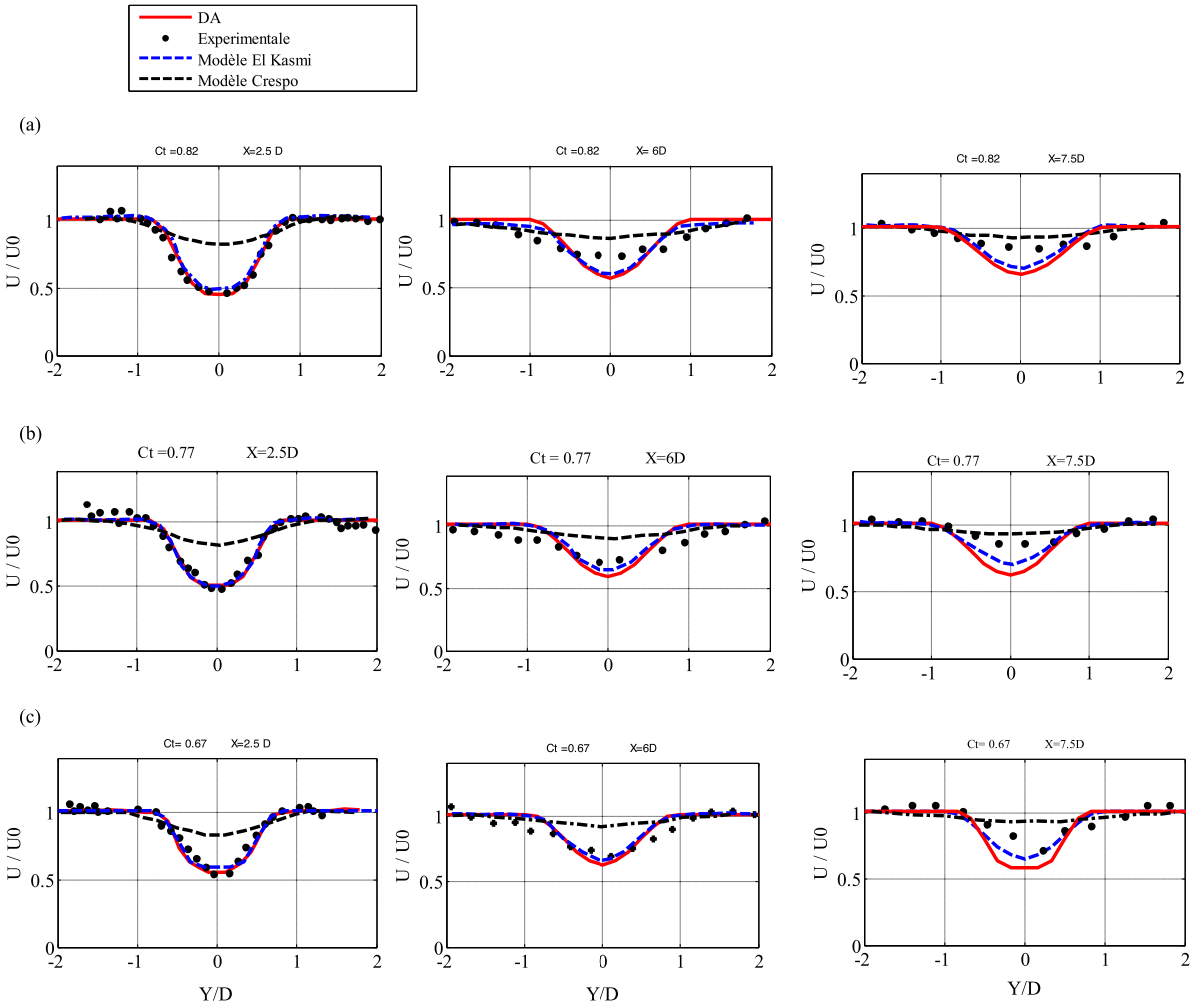

Fig. 16. Comparison of the deficit profiles of the actuator volume with El Kasmi model for the Nibe 630 kW for Ct = 0.82; Ct = 0.77 and Ct = 0.67 at X = 2.5, 6, and 7.5D.

with Crespo's wake model [41]. The approach proposed by A. El Kasmi and C. Masson [22] has allowed reducing the turbulent kinetic energy production rate (P_k) in order to preserve, as a result, the axial velocity deficit in the wake.

In the present work, we notice that the consideration of an actuator volume with a specific thickness (in an explicit formulation) makes it possible to increase the dissipation ε in the region of the shear and that without modification of the turbulent energy production (Pk.) terms. Indeed, we observe that the direct effect of the rotor thickness on the flow is an immediate reduction of the turbulent viscosity (μt) involving moderation of the turbulence production (Pk). The slowing down of the turbulent viscosity recovery then tends to preserve the axial speed deficit over a longer distance and allows thus to maintain and reproduce the wake downstream the rotor.

These results are in accordance with the comparative study of E. Réthoré [44] that applied various dissipation constants ($C\varepsilon 4 = 0.001$, $C\varepsilon 4 = 0.005$ and $C\varepsilon 4 = 0.1$) to a region ranging from −D to + D around the rotor with zero actuator disc thickness. It has been shown that the increase in the region size where the dissipation rate is applied has the same effect as the model constants increase.

It should also be noted that the depth of the actuator volume choice in D-VA model remains critical as to the improvement of the wake results. In fact, a parametric study using four-disc thicknesses ΔX reveals a direct effect on the evolution (i) of the dissipation, (ii) the turbulent kinetic energy and (iii) the deficit of the axial speed depicted

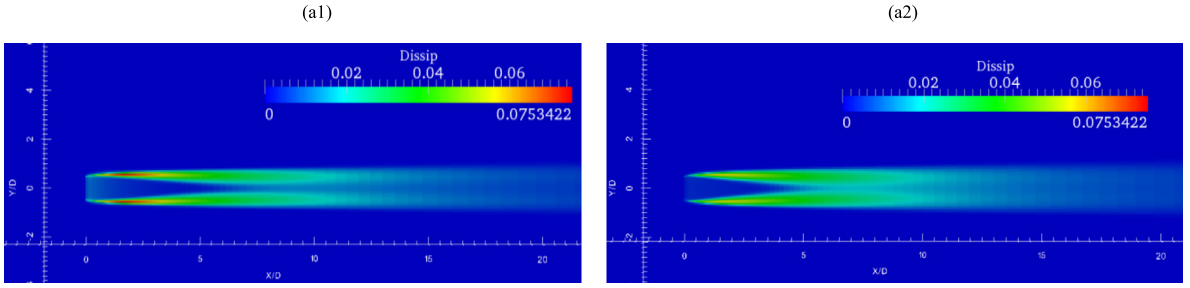

Fig. 17. Distribution of the dissipation—Nibe 630 kW($U_0 = 8.54$, Ct = 0.82) ; (a1) ΔX1 (a2) ΔX3.

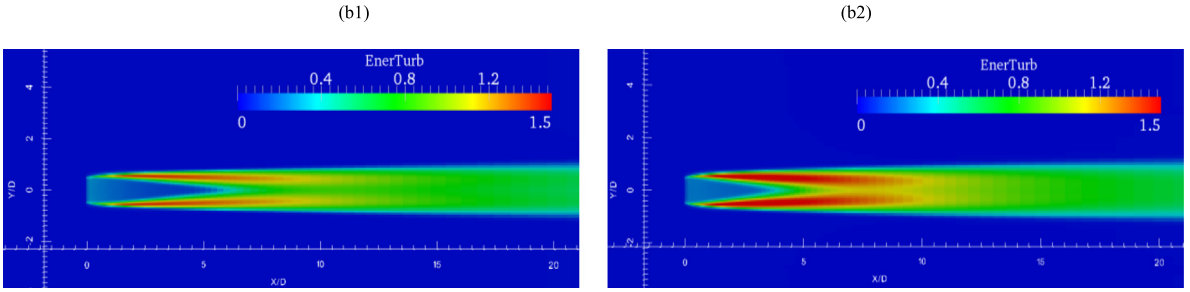

Fig. 18. Distribution of the turbulent kinetic energy—Nibe 630 kW($U_0 = 8.54$, Ct = 0.82) ; (b1) ΔX1 and (b2) ΔX3.

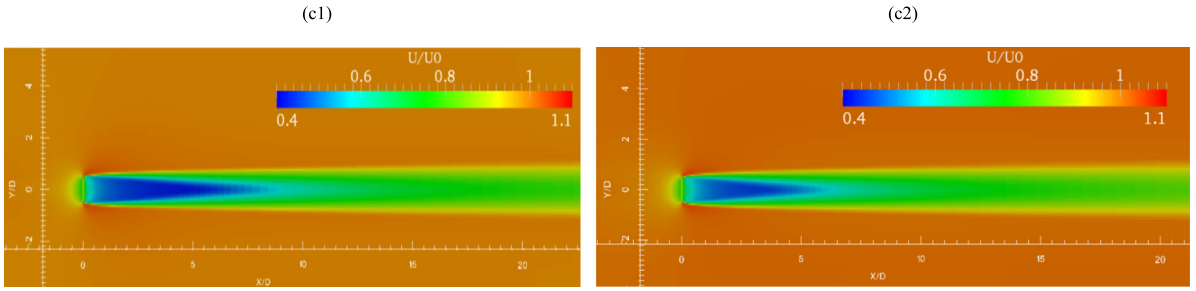

Fig. 19. Distribution of the velocity field—Nibe 630 kW ($U_0 = 8.54$, Ct = 0.82) ; (c1) ΔX1 and (c2) ΔX3. (For interpretation of the references to colour in this figure legend, the reader is referred to the web version of this article.)

respectively in Figs. 17–19. Only the results obtained with ΔX1 = 0.38 m and ΔX3 = 0.78 m corresponding to 8% and 16% of the blade span are presented here.

The distributions of the dissipation (Fig. 17(a2)), the turbulent kinetic energy (Fig. 18(b2)) and the velocity field (Fig. 19(c2)) obtained for the thickness (ΔX3) show a wake distribution in better agreement with the experimental data.

We observe that when the actuator volume thickness being closer to the maximum cord of the turbine, it permits to accurately reproduce the deficit area of the near wake and to reduce the difference in speed in the far wake. It should be noted that the results obtained for a thickness of the actuator volume ΔX4 = 1 m are similar to those of ΔX3. The comparison results show that the consideration of an actuator volume with a certain thickness behaves almost similar to the increase of the dissipation constant as affirmed by [44]. Indeed, unlike the classical actuator disc model, the D-VA model, in its explicit formulation let to preserve the axial velocity deficit over a longer distance, but its adaptation requires an adequate estimate of the rotor thickness.

3.2.8. The axial profiles in the centre axis of the rotor

Fig. 20 compares the wake results obtained with different disc thicknesses, defined by the relation (ΔX = E (1+ sin (B))), where E is the blade depth determined according to the average cord as c = 7.5%, 9%, 16% and 20% of

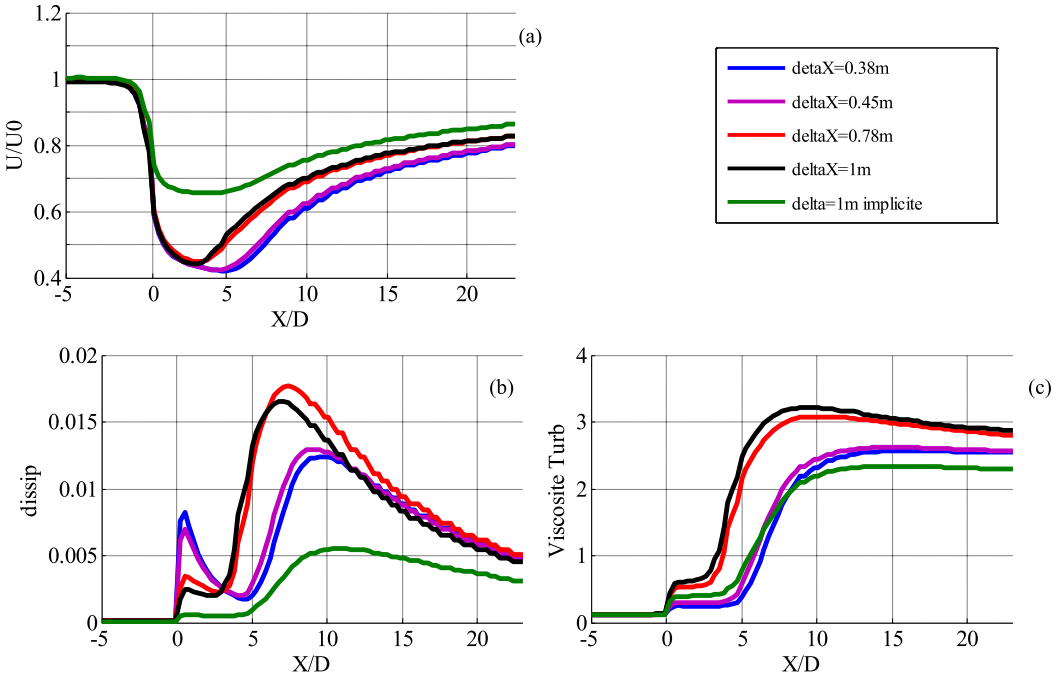

Fig. 20. The normalized velocity (a), the dissipation (b) and the turbulent viscosity (c) in the centre axis of the rotor y = 0, for different thicknesses of the actuator volume for the Nibe 630 kW ($U_0 = 8.54$ m/s, Ct = 0.82).

the blade span, allowing to obtain different corresponding volume thicknesses of $\Delta X1 = 0.38$ m, $\Delta X2 = 0.45$ m, $\Delta X3 = 0.78$ m and $\Delta X4 = 1$ m.

The profiles depicted in Fig. 19 represent the normalized axial velocity in (a), the dissipation ε in (b) and the turbulent viscosity μt in (c) obtained with the D-VA model applied in the explicit formulation and compared to the implicit solution for $\Delta X4 = 1$ m (in green). One can see that the plots of different parameters are extremely close for ($\Delta X1 = 0.38$ m and $\Delta X2 = 0.45$ m) and for ($\Delta X3 = 0.78$ m and $\Delta X4 = 1$ m). The common point showed by Fig. 20(a) is the gradual decrease of the axial velocity to achieve an inflection point where the wake begins to recover in far wake. However, we note that this inflection point is overestimated by the results of $\Delta X1$ and $\Delta X2$ where the near wake depth is shifted to X = 5D with a minimum deficit of $U/U_0 = 0.42$ while the experimental deficit data is around 0.48 [32]. This overestimation is due to a reduced actuator volume thickness acting as a singular perturbation, which induces an excessively large dissipation around the wake zone. This maximum dissipation does not appear in Fig. 20(b) due to the central position of the data extraction line but Fig. 19(c) shows a slowing down of turbulent viscosity recovery caused by high dissipation and leading to a longer wake recovery delay.

The simulations results obtained by $\Delta X3$ and $\Delta X4$ in explicit formulation show an inflection point in agreement with the experimental recordings of the near wake with a minimum deficit of about $U/U_0 = 0.46$ achieved around X = 3D with a relative error of 1.6%.

Otherwise, the results obtained by the actuator volume in implicit formulation within a thickness of 1 m, show a slight decrease in the axial speed around 68% while the inflection point is still located at X = 3D downstream of the rotor. The improvement of the dissipation rate (Fig. 19(b)) in this case, allows to keep the speed deficit longer but without reaching the required minimum value.

In the far region, a relatively extended recovery of the wake is recorded with 84% of its initial value reached by $\Delta X3$ and $\Delta X4$ in explicit formulation but the natural return to the reference speed is faster for the implicit simulation with $\Delta X4$. Note that the far wake delay occurs in must numerical studies, even in the full simulation. Indeed, the maximum recovery obtained by the LES simulations achieved a maximum of 90% [44,47].

The closest results of the experimental data are obtained by the actuator volume relative to $\Delta X3 = 0.78$ m, that are used in the D-VA model validation for the Nibe B turbine (Section 3.2.4).

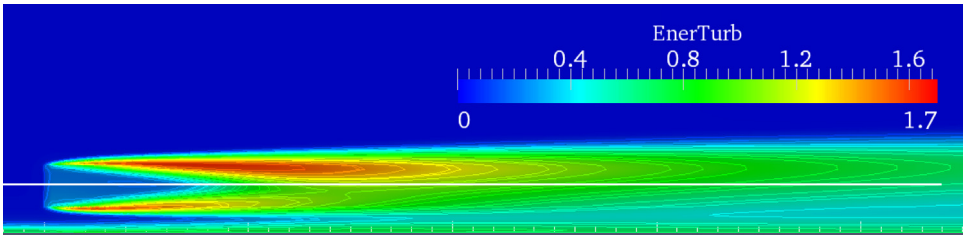

Fig. 21. Spatial distribution of turbulent kinetic energy in the vertical plane (x, z) for Nibe 630 kW ($U_0 = 8.54$ m/s and Ct = 0.82 and It = 11%).

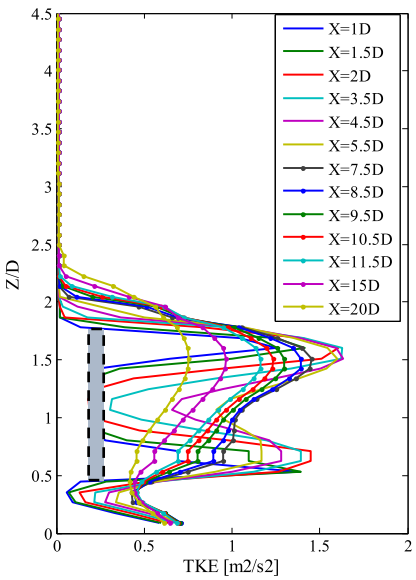

Fig. 22. Vertical profiles of turbulent kinetic energy at different positions downstream the Nibe 630 kW (U0 = 8.54 m/s and Ct = 0.82 and It = 11%) in the plane of the rotor.

3.2.9. Turbulent kinetic energy

The turbulent kinetic energy distribution following (x, z) obtained with the D-VA model for the Nibe B with ΔX3 are shown in Fig. 21 and the vertical profile variations at different positions downstream of the rotor are shown in Fig. 22. They indicate that the shear layer has maxima of kinetic energy on both sides of the near wake zone, but a higher turbulence peak is recorded in the upper rotor section. This result is qualitatively in agreement with the observations of Porté Agel et al. [47], which describe similar peaks at the blade tips obtained by the non-uniform actuator disc method combined with the LES resolution. The spatial distribution (Fig. 21) shows that the maximum of kinetic energy propagates downstream to a distance of 3-4D, and then mixes with the flow to form a global shear layer concentrated at above the rotor symmetry axis. This phenomenon confirmed by the evolution of turbulent kinetic energy profiles presented at different positions in the wake in Fig. 22. The increase in turbulent kinetic energy in the near region is mainly pronounced at the positions of X = 1D up to X = 4D with two peaks on each side of the axis, visibly higher than the high side of the rotor.

The two peaks merge and then gradually decrease to form the far wake profiles. This difference between the rotor borders illustrates the non-symmetry of the flow due to soil effects and the atmospheric incident wind flow.

3.3. Comparison of full rotor simulation with the generalized actuator volume model

The results of the D-VA model are compared with those of the complete Nibe 630 kW simulation, it should be noted that because of simulations parameters that are not identical, the comparison between the two approaches is

Table 6. Comparison of full rotor simulation with generalized actuator volume for Nibe 630 kW.

	Full rotor simulation	Actuator volume D-VA
Inlet condition	$U_0 = 8.54$ m/s	Profile CLA (U(z), k(z), ε(z))
Geometry	Exact blade shape	A simple volume of D and Δ X3
Grid	3.5 Million cells	0.784 559 cells
Rotate domain	+++	−−−
Interface model	+++	−−−
CPU time	305 h	3 h
Iteration number	40 000	2000
Complexity	+++	+
Scale of detail	+++	+

not so obvious. Indeed, the full simulations are in an unsteady state, considering a homogeneous incoming flow, without taking into account the soil effects, while for the generalized model the average calculation is steady state within an atmospheric incoming flow. Nevertheless, the reference speed at the hub and the turbulence intensity are the same, but the comparison given in Table 6 remains only qualitative.

Note that the full simulation necessitates a strongly large CPU time with huge cells numbers compared to the simplified hybrid D-VA model that lets to obtain reasonable wake results in less time.

4. Conclusion

This study illustrated that wake analysis is of crucial interest to improve wind farm performance. Indeed, the (U-RANS) simulation of the flow around a rotating wind turbine confirmed that the wake zone is characterized by strong velocity gradients and significant turbulence increase, which obviously affects wind energy production of adjacent wind turbines, notably those installed in the wake axis. However, although the wake dynamics downstream the rotor was substantially well reproduced by the full simulations, the mobile mesh calculation seems to be inadequate for the wake investigation of several wind turbines. This calculation completion was accompanied by several constraints related mainly to the long CPU time. Furthermore, the fluid flow connectivity between Rotor/Stator domains remains particularly sensitive to the interface discretization and that does not allow, nowadays, studying the wake of several wind turbines in relative motion. For this purpose, a simplified generalized wake model (D-VA) was developed and validated with experimental data. The parametric study of the actuator volume has demonstrated that the disc thickness consideration improves the flow dissipation rate and allows keeping the speed deficit longer in the axis. The joining of this principle with an explicit formulation made it possible to improve the wake prediction. The validation series have shown the capacity of the proposed generalized actuator volume model to forecast the wake in wind farm. Indeed the results obtained were close to the experimental data of the Nibe B and the Danwin turbine and were nearly similar to those obtained by El Kasmi and Masson model. With the objective of analysing the deficit zone downstream of the rotor, the proposed D-VA model offers an acceptable prediction of the large-scale wake in wind farm.

References

[1] Hansen AD, Hansen LH. Wind turbine concept market penetration over 10 years (1995–2004). Wind Energy 2007;10(1):81–97.
[2] Sanderse B. Aerodynamics of wind turbine wakes - literature review. Technical report ECN-E–09-016, Netherlands: ECN; 2009.
[3] Castellani F, Astolfi D, Mana M. Investigation of terrain and wake effects on the performance of wind farms in complex terrain using numerical and experimental data. Wind energy 2017;20(7):1277–89.
[4] Hansen MOL, Sørensen JN, Voutsinas S, Sørensen N, Madsen HA. State of the art in wind turbine aerodynamics and aero elasticity. Prog Aerosp Sci 2006;42(4):285–330.
[5] Crespo A, Hernández J, Frandsen S. Survey of modelling methods for wind turbine wake and wind farms. Wind Energy 1999;2(1):1–24.
[6] Vermeer LJ, Sørensen JN, Crespo A. Wind turbine wake aerodynamics. Prog Aerosp Sci 2003;39(6):467–510.
[7] Troldborg N, Sørensen JN, Mikkelsen R. Actuator line simulation of wake of wind turbine operating in turbulent inflow. J Phys Conf Ser 2007;75(1). 012063.
[8] Sanderse B, van der Pijl Sp, Koren B. Review of computational fluid dynamics for wind turbine wake aerodynamics. Wind Energy 2011;14(7):799–819.
[9] Göçmen T, van der Laan P, Réthoré P-E, Diaz AP, Larsen GC, Ott S. Wind turbine wake models developed at the technical university of Denmark: A review. Renew Sustain Energy Rev 2016;60:752–69.

[10] Thé J, Yu H. A critical review on the simulations of wind turbine aerodynamics focusing on hybrid RANS-LES methods. Energy 2017;138:257–89.
[11] Glauert H. Aerodynamic theory, vol. 4. Berlin, Germany: Julius Springer; 1935, p. 169–360.
[12] Mikkelsen R. Actuator disc methods applied to wind turbines. In: Fluid mechanics. Lyngby: Department of Mechanical Engineering, Technical University of Denmark; 2003.
[13] Dobrev I, Massouh F, Rapin M. Actuator surface hybrid model. In: The science of making torque from wind. Journal of physics: conference series, vol. 75, Lyngby, Denmark; 2007.
[14] Makridis A, Chick J. Validation of a CFD model of wind turbine wakes with terrain effects. J Wind Eng Ind Aerodyn 2013;123:12–29, Part A.
[15] Sørensen JN, Myken A. Unsteady actuator disc model for horizontal axis wind turbines. J Wind Eng Ind Aerodyn 1992;39:139–49.
[16] Sørensen JN, Shen WZ, Munduate X. Analysis of wake states by a full-field actuator disc model. Wind Energy 1998;1:73–88.
[17] Masson C, Smaïli A, Leclerc C. Aerodynamic analysis of HAWTs operating in unsteady conditions. Wind Energy 2001;4:1–22.
[18] Ammara I, Leclerc C, Masson C. A viscous three-dimensional method for the aerodynamic analysis of wind farms. J Sol Energy Eng 2002;124:345–56.
[19] F J. Ainslie development of an eddy viscosity model for wind turbine wakes. In: Garrad A editor. Proceedings of the 7th BWEA wind energy conference. Oxford, UK; 1985, p. 61–6.
[20] Alinot C, Masson C. k-ε model for the atmospheric boundary layer under various thermal stratifications. J Sol Energy Eng 2005;127:438–43.
[21] Sibuet Watters C. Étude numérique du sillage tourbillonnaire d'une éolienne [Ph.D.], Montréal: École de Technologie Supérieure; 2008.
[22] El Kasmi A, Masson C. An extended model for turbulent flow through horizontal-axis wind turbines. J Wind Eng Ind Aerodyn 2008;96(1):103–22.
[23] Sørensen NN, Hansen MOL. Rotor performance predictions using a Navier–Stokes method. 1998, AIAA Paper, 98–0025.
[24] Johansen J, Sørensen NN, Michelsen JA, Schreck S. Detached-eddy simulation of flow around the NREL phase VI blade. Wind Energy 2002;5:185–97.
[25] Zahle F, Sørensen NN. Overset grid flow simulation on a modern wind turbine. 2008, AIAA Paper 2008–6727.
[26] Code_Saturne : Edf's general-purpose CFD software, user meeting. 2013.
[27] Code_Saturne30. http://code-saturne.org.
[28] Patankar S. Numerical heat transfer and fluid flow. 1980.
[29] Jourieh M. Développement d'un modèle représentatif d'une éolienne afin d'étudier l'implantation de plusieurs machines sur un parc éolien [Doctorat thesis], L'ENSAM; 2007.
[30] Hansen MOL. Aerodynamics of wind turbines. Earthscan; 2013.
[31] Taylor GJ, Smith D. Wake measurements over complex terrain. In: Proc. 13 Th BWEA wind energy conf. UK; 1991. p.335–42.
[32] Taylor GJ, Milborrow DJ, McIntosh DN, Swift-Hook DT. Wake measurements on the Nibe windmills. In: Proceedings of seventh BWEA wind energy conference. Oxford; 1985, p. 67–73.
[33] AbdelSalam AM, Ramalingam V. Wake prediction of horizontal-axis wind turbine using full-rotor modeling. J Wind Eng Ind Aerodyn 2014;124:7–19.
[34] Carcangiu CE. CFD-RANS study of horizontal axis wind turbines [Doctoral thesis], Universita' Degli Studi di Cagliari; 2008.
[35] Laan M. An improved k- ϵ model applied to a wind turbine wake in atmospheric turbulence. Wind Energy 2015;18(5):889–907.
[36] Sumner J, Watters CS, Masson C. CFD in wind energy: The virtual multiscale wind tunnel. Energies 2010;3(5):989–1013.
[37] Salman Siddiqui M, Rasheed Adil, Kvamsdal Trond. Influence of tip speed ratio on wake flow characteristics utilizing fully resolved CFD methodology. IOP Conf Ser: J Phys Conf Ser 2017;854. 012043.
[38] R éthoré P-E, Sørensen NN, Zahle F. CFD model of the MEXICO wind tunnel.
[39] España G, Aubrun S, Loyer S, Devinant P. Wind tunnel study of the wake meandering downstream of a modelled wind turbine as an effect of large scale turbulent eddies. J Wind Eng Ind Aerodyn 2012;101:24–33.
[40] Magnusson M, Rados KG, Voutsinas SG. A study of the flow downstream of wind turbine using measurements and simulations. Wind Eng 1996;20(6):389–403.
[41] Crespo A, Manuel F, Moreno D, Fraga E, Hernandez J. Numerical analysis of wind turbine wakes. In: Proceedings of Delphi workshop on wind energy applications. Delphi, Greece; 1985. p. 15–25.
[42] Crespo A, Hernandez J, Fraga E, Andreu C. Experimental validation of the UPM computer code to calculate wind turbine wakes and comparison with other models. J Wind Eng Ind Aerodyn 1988;27(1–3):77–88.
[43] Hussein AS, El-Shishiny HE. Modeling and simulation of micro-scale wind farms using high-performance computing. Int J Comput Methods 2012;09(02). 1240025.
[44] Réthoré E. Wind turbine wake in atmospheric turbulence. Aalborg at Aalborg, Denmark: RisøDTU; 2009.
[45] Troldborg N, Sørensen JN, Mikkelsen R. Actuator line simulation of wake of wind turbine operating in turbulent inflow. J Phys Conf Ser 2007;75(1). 012063.
[46] Chen YS, Kim SW. Computation of turbulent flow using an extended turbulence closure Model. NASA Contractor Report, NASA CR-179204, 1987.
[47] Porté-Agel F, Wu Y-T, Lu H, Conzemius RJ. Large-eddy simulation of atmospheric boundary layer flow through wind turbines and wind farms. J Wind Eng Ind Aerodyn 2011;99(4):154–68.